ORIGINAL PAPER

Thermal evolution and the maturation of the deeply buried lower Paleozoic source rocks in the Tarim Basin, northwest China

Yuchen Liu[1,2] · Suying Dong[1] · Changhong Zhao[1]

Abstract

The Ordovician reservoirs in the Tarim Basin have shown good exploration potential in recent years. To better understand its complex thermal history and further oil and gas exploration, we reconstructed the thermal evolution of the lower Paleozoic strata in Tarim Basin by applying new and previously published equivalent vitrinite reflectance (Requ), (U–Th)/He ages, and fission tracks. The modeled results indicated that there were three phases of heat flow evolution in the Tarim Basin: (1) The gradual cooling stage during Carboniferous-Ordovician, the heat flow was gradually decreasing during this period; (2) Rapidly raised stage in the early Permian period, the heat flow in Tabei and Tazhong uplift was raised rapidly during this period and the maximum is 51~62 mW/m^2; (3) The decline stage since Middle Permian. The tectonic activity was relatively stable and the heat flow was gradually reduced during this period. The abnormal high temperature of the Permian may be the result of the magmatic activity events. Additionally, the maturity evolution plane distribution of the bottom interface of the Lower Cambrian source rock was modeled based on the new thermal histories, suggesting that the source rocks experienced rapid heating during the Caledonian period, and entered the hydrocarbon generation stage at the end of Ordovician. In the end of Mesozoic, the Cambrian source rocks reached the dry gas stage in the south of Shuntuoguole low uplift, Manjiaer depression, Tadong uplift, and Kongquehe slope. Currently, the maturity mostly maintained the characteristics of the end of the Mesozoic. The thermal history and maturity histories of the lower Paleozoic source rock in Tarim Basin provide new insights to guide oil and gas exploration of the basin.

Keywords Paleothermal indicator · Thermal history · (U–Th)/He ages · Low temperature thermochronology · Tarim Basin

Introduction

Due to the improvements in exploratory drilling techniques and promotions in the exploration activities, oil and gas in deep and ultra-deep strata have been a hot topic in both research and exploration and it will be the most important field for raising reserves in the future (Dyman et al. 2002; Bai and Cao 2014; Liu et al. 2018; Yao et al. 2018; Liu et al. 2020a). Significant breakthroughs and discovery of oil and gas

resources have been made recently in the Ordovician formations characterized by a burial depth of more than 6300m of Tarim Basin, providing a new resource target for deep and ultra-deep oil and gas exploration of Western China (Zhu et al. 2018; Zhou et al. 2019; Qi 2016; Wang et al. 2014; Liu et al. 2020b; Yang et al. 2020).

The thermal history of source rocks is of vital importance to the evaluation of source rocks, which controls the timing of hydrocarbon generation and expulsion (Pang et al. 2012; Carminati et al. 2010; Hudson and Hanson 2010; Kosakowski and Krzywiec 2013). The hydrocarbon source rocks in the Tarim Basin are mainly found in the lower Cambrian and lower Ordovician strata characterized by a burial depth of more than 6500m (Li et al. 2015; Cai et al. 2015; Chang et al. 2014a, b; Zhang et al. 2005; Zhang et al. 2014; Wang et al. 2010). They have the characteristics of high abundance of organic matter (the total organic carbon (TOC) content is 0.5–3.36 wt%, average TOC content = 2.84 wt%; Sun et al. 2003) with the kerogen type of I–II, and the degree of

---

✉ Yuchen Liu
liuyuchen.2010@163.com

1 College of Geosciences, Northeast Petroleum University, Daqing 163318, Heilongjiang, China

2 Northeast Petroleum University, Daqing 163318, Heilongjiang Province, P. R. China

thermal evolution is currently in the high-over mature stage (Zhu et al. 2016; Zheng et al. 2018; Xiong et al. 2015; Qi 2016; Yan et al. 2020; Wang et al. 2006). The black and dark-gray Cambrian-Ordovician mudstones are both relatively high-quality source rocks and they are the major source rocks for the Ordovician reservoirs (Mu 2009; Zhang et al. 2005), whereas there is no consensus on the contribution of these two sets of source rocks to the hydrocarbon in Ordovician reservoirs. The main reason for the dispute of the consistency of thermal history in the Tarim Basin has been difficult to reach. Some scholars believed that the geothermal gradient of Tarim Basin had shown a gradual decline since the early Paleozoic, with relatively higher values in the central and eastern regions (Qiu et al. 2011, 2012; Liu et al. 2019; Chang et al. 2014a, b), while others argued that due to the influence of magmatic activity, the peak geothermal gradient appeared in the Carboniferous-Permian of Tabei and Tazhong uplift (Li et al. 2010; Li et al. 2016; Yu et al. 2010; Xiang et al. 2013). Uncertainty about the thermal history and the maturity evolution of lower Paleozoic has restricted further oil and gas exploration in the Tarim Basin.

In this study, we combined a large number of new and previously published equivalent vitrinite reflectance (Requ), (U–Th)/He ages, and fission tracks to analyze the tectono-thermal evolution of different tectonic units in Tarim Basin,

and modeled the thermal evolution of the Cambrian-Ordovician source rocks. In addition, based on the occurrence state of Ordovician oil and gas reservoirs, the main source rocks are defined from the perspective of thermal evolution of source rocks. This study has an important guiding significance for hydrocarbon exploration in the Tarim Basin.

Geological setting

The Tarim Basin is the largest hydrocarbon-bearing basin in the northwest of China (Fig. 1a) and has an area of 560×10^3 km^2. The basin is bounded by the Tian Shan Mountains to the north, the Kulugetake Mountains to the northeast, the Kunlun Mountains to the southwest, and the Altun Mountains to the southeast (Jia 1997; Qiu et al. 2012; Tang et al. 2004) (Fig. 1b). The basin can be subdivided, based on basement morphology, major faults, structural deformation, and sediment distribution, into several structural zones, including five depressions (i.e., the Kuqa depression, the Awati sag, the Manjiaer sag, the Tanggu depression, the Southwestern depression belt), five uplift regions (the Tabei uplift belt, the Shuntuoguole low rise, the Tazhong uplift belt, the Bachu uplift belt, and Tadong uplift), and two slopes (the
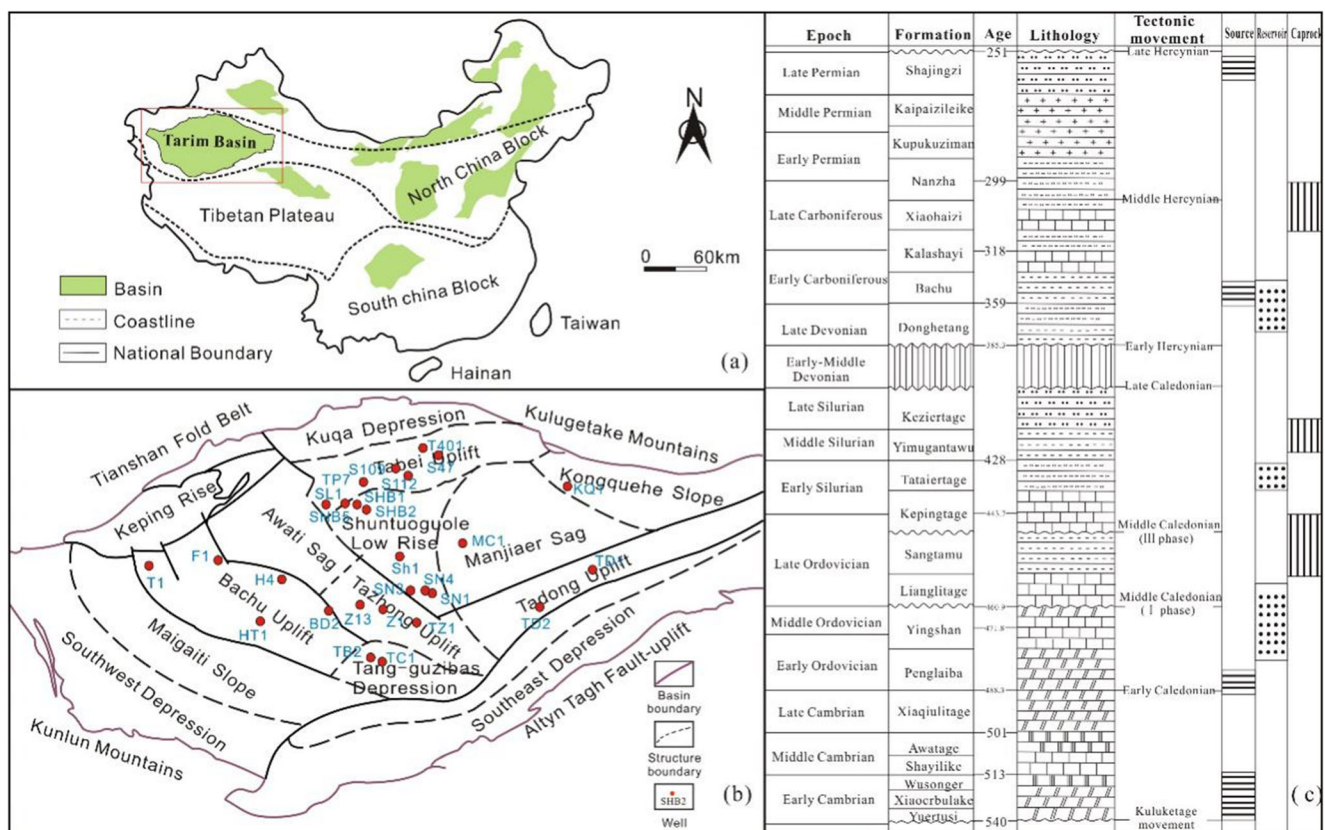

Fig. 1 (a) A simplified view of the outline of China, (b) Simplified distribution map of the tectonic units in Tarim Basin, (c) Paleozoic stratigraphy of the Tarim Basin (derived from exploration and production research institute of Northwest Oilfield Branch Company, SINOPEC)

Kongquehe slope and the Maigati slope) (Ma et al. 2015; Jia and Wei 2002) (Fig. 1b).

The Tarim Basin has experienced five stages of tectonic evolution: basement formation stage, the Cryogenian-Ediacaran strong extension-compression stage, Cambrian-Ordovician weak extension-strong compression stage, Silurian-Cretaceous fluctuation and migration stage, and Cenozoic weak extension-strong compression stage. The Tarim Basin was initially formed in the middle and late Ordovician, and ancient Kunlun Ocean was subducted beneath the Tarim block. The strong squeezing force from the SW direction resulted in the formation of the Tazhong uplift (Li et al. 2013; Ren et al. 2011, 2012). From Silurian to Devonian, after the Kunlun Caledonian collision orogeny was ended, the Paleo-Tethys Ocean was developed (Yang et al. 2005). Synchronously, intense folding orogeny occurred in the Arkin tectonic domain (Liu et al. 2007), and some parts of the top of the Silurian and Devonian units in the northern of the Tarim Basin were eroded and truncated, which resulted in the transformation of the tectonic framework from the west part being higher than the east part to the east part being higher than the west part (Ding et al. 2009).

Cambrian and Ordovician strata constitute a complete source-reservoir-caprock assemblage in the Tarim Basin (from bottom to top: Yuertusi Formation, Penglaiba Formation, Yingshan Formation, Yifangfang Formation, and Sangtamu Formation) (Fig. 1c). Yuertusi Formation of the Lower Cambrian is widely developed in Tazhong uplift, which is mainly deposited within black mudrock. The Upper Cambrian-Lower Ordovician source rock is only distributed in the Mandong sag. The source rocks of the lower Cambrian are sapropelic, approximately 150–350m in thickness, and with total organic carbon (TOC) content of more than 1% (Wu et al. 2016; Chen et al. 2018), and the Upper Cambrian-Lower Ordovician source rock is also sapropelic with a TOC of 2.84% and an average thickness of 110m (Bao et al. 2018; Yu and Zhou 2005). Yijianfang and Yingshan Formations are mainly composed of mudstone and limestone, and the cracks and dissolved pores are relatively developed, which are good reservoirs. The thick mudstone layers of the Upper Ordovician Santamu Formation are stably distributed in the area and are good area caps.

Methods and samples

Methods

To enhance the accuracy of thermal history, the equivalent vitrinite reflectance (Requ), (U–Th)/He ages of apatite and zircon, and fission tracks of apatite and zircon were combined to simulate the thermal history of the Tarim Basin. Different models were used for different paleo-thermal indicators, the

Easy %Ro model for Requ (Sweeney and Burnham 1990), the multi-component dynamic model for AFT ages (Ketcham et al. 2007), the parallel curvilinear model for ZFT ages (Yamada et al. 2007), the Farley model for AHe (Farley 2000), and the Reiners model for ZHe (Reiners et al. 2004). Our database contains 258 sets of vitrinite reflectance (Ro), 66 sets of (U–Th)/He ages for apatite and zircon (Table 1), and 52 sets of apatite fission tracks (Table 2), and these samples are distributed in Tabei uplift, Tazhong uplift, Shuntuoguole low uplift, Tanggu depression, Kongquehe slope, Tadong uplift, Bachu uplift, Awati sag, which have well representative and relatively scattered locations covering most area of the Tarim Basin.

(U–Th)/He ages

The (U–Th)/He analyses of apatite and zircon were conducted at the School of Earth Science in University of Melbourne. The (U–Th)/He analyses were conducted following the procedures described by Gleadow et al. (2015). The extraction and measurement of helium (He) from a single crystal was followed by the measurement of U and Th by isotope dilution, Parr bomb dissolution, and high-resolution inductive-coupled plasma mass spectrometry (HR-ICPMS). The helium extraction involves laser heating of crystals inside Nb foil packets to a temperature of approximately 1300 °C for two to four 10-min extraction. Zircon He ages were calculated and corrected for α-emission following the approach of Farley et al. (1996). A total of nine zircon samples were tested to obtain (U–Th)/He ages. Three replicate analyses per sample were tested for all samples. The other (U–Th)/He ages for apatite and zircon samples were obtained from previous studies (Qiu et al. 2011, 2012).

Vitrinite reflectance

We compiled 258 vitrinite reflectance (Ro) or Requ values from 20 wells in the Tarim Basin. Vitrinite reflectance (Ro), bitumen reflectance (Rb), and vitrinitelike reflectance (Rv) of eight wells in Shuntuoguole low uplift were measured from dark mudstone at the China University of Petroleum, Beijing. Due to the lack of vitrinite originating from higher plants in the Lower Paleozoic, Requ data are converted from Rb or Rv, and Requ was used to study the maturity of lower Paleozoic. There are several formulae for obtaining Requ from Rb, which corresponds to different maturity stages (Jacbo 1989; Liu and Shi 1994; Petersen et al. 2009; Qiu et al. 2012; Xiao et al. 2000). The formulae for converting Requ from bitumen reflectance and vitrinite-like maceral reflectance in this study are used by Xiao et al. (2000). The other Requ data for Tabei uplift, Tazhong uplift, Tang-gu depression, Bazhu uplft, and Tadong uplift were obtained from previous studies (Wang et al. 2010; Liu et al. 2016; Li et al. 2016; Qiu et al. 2012).

Table 1 The tested (U–Th)/He ages of apatite and zircon samples in Tarim Basin

Tectonic unit	No.	Samples	Strata	Mineral	Depth (m)	Mass (mg)	4He (nmol/g)	Th/U	U (ppm)	Th (ppm)	Ft	Corrected age (Ma)	Error (±1σ)	eU (ppm)	Data sources
Shuntuoguole area	1	ST1-5a	D	Zircon	4542	4.9	0.038111	0.87	127.6	111.1	0.78	398	24.7	153.7	This study
	2	ST1-5b	D	Zircon	4542	3.7	0.020224	0.72	114	82.6	0.74	330.6	20.5	133.4	This study
	3	ST1-5c	D	Zircon	4542	3.4	0.011479	1.33	43.4	57.8	0.73	471.5	29.2	57	This study
	4	ST1-6a	S	Zircon	5100	7.5	0.150692	0.55	416	230.7	0.8	341.7	21.2	470.3	This study
	5	ST1-6b	S	Zircon	5100	3.7	0.033068	0.9	140.8	126.4	0.74	417.2	25.9	170.5	This study
	6	ST1-6c	S	Zircon	5100	2.8	0.012727	0.82	82.6	67.8	0.72	364.2	22.6	98.5	This study
	7	ST1-7a	S	Zircon	5786	7.5	0.016537	0.5	227.3	113.1	0.77	71.1	4.4	253.9	This study
	8	ST1-7b	S	Zircon	5786	11.9	0.050496	0.42	110.6	46.4	0.81	279.8	17.3	121.5	This study
	9	ST1-7c	S	Zircon	5786	7.5	0.047335	1.2	198.5	237.5	0.77	200.5	12.4	254.4	This study
	10	SHB5-2a	S	Zircon	5212	5	0.00763	0.61	30.8	18.7	0.75	344.9	21.4	35.2	This study
	11	SHB5-2b	S	Zircon	5212	3.2	0.011264	0.92	100.5	92.1	0.72	234.4	14.5	122.1	This study
	12	SHB5-2c	S	Zircon	5212	1.9	0.009194	1.18	88.8	104.7	0.69	342.9	21.3	113.4	This study
	13	SHB5-3a	S	Zircon	5928	2.2	0.009945	0.3	85.1	25.2	0.71	401.3	24.9	91	This study
	14	SHB5-3b	S	Zircon	5928	3.8	0.030314	0.67	155.5	104.1	0.76	354.7	22	180	This study
	15	SHB5-3c	S	Zircon	5928	2	0.01962	0.61	166.8	101.5	0.7	406.2	25.2	190.7	This study
	16	SHB5-4a	S	Zircon	6766	1.5	0.023735	0.79	280.2	220.1	0.66	390.6	24.2	331.9	This study
	17	SHB5-4b	S	Zircon	6766	1.5	0.017446	0.24	384.1	90.9	0.68	224.3	13.9	405.5	This study
	18	SHB5-4c	S	Zircon	6766	2.8	0.025579	1.03	93.5	96.2	0.71	620.1	38.4	116.1	This study
Awati sag	19	AD1-3a	P	Zircon	5199	1.8	0.011478	0.6	168.7	101.4	0.69	267.1	16.6	192.5	This study
	20	AD1-3b	P	Zircon	5199	2.4	0.031866	0.62	221	137.9	0.7	418.4	25.9	253.4	This study
	21	AD1-3c	P	Zircon	5199	1.9	0.008455	0.52	128.8	67.3	0.66	247.2	15.3	144.6	This study
	22	AD1-4a	D	Zircon	5995	5.3	0.028886	0.85	95.2	81.2	0.77	376.9	23.4	114.3	This study
	23	AD1-4b	D	Zircon	5995	3.8	0.028565	1.15	115.1	132.2	0.75	411.4	25.5	146.2	This study
	24	AD1-4c	D	Zircon	5995	3.7	0.062978	1.12	142.3	159.5	0.73	717.4	44.5	179.8	This study
	25	AD1-5a	S	Zircon	6357	3.5	0.009497	2.08	43.5	90.5	0.73	337.6	20.9	64.8	This study
	26	AD1-5b	S	Zircon	6357	2.5	0.033913	0.94	249.3	234.5	0.7	355.3	22	304.4	This study
	27	AD1-5c	S	Zircon	6357	4.5	0.032603	0.67	97.2	64.9	0.76	504.6	31.3	112.5	This study
Tazhong uplift	28	Z2-1a	K	Apatite	2085	4.82	0.1179	0.54	11.23	5.87	0.75	21.08	0.42	12.63	Qiu et al. (2012)
	29	Z2-2a	Tr	Apatite	2553	2.36	8.854	2.41	117.1	275.02	0.67	251.12	6.95	181.73	Qiu et al. (2012)
	30	Z2-3a	Tr	Apatite	2963	4.2	1.29	3.05	15.25	45.27	0.73	132.34	2.05	25.89	Qiu et al. (2012)
	31	Z2-6a	P	Apatite	3972	1.39	0.15	1.12	249.44	272.51	0.64	4.52	0.09	313.48	Qiu et al. (2012)
	32	Z2-8a	D	Apatite	4804	9.93	0.043	3.48	7.43	25.19	0.79	3.35	0.12	13.35	Qiu et al. (2012)
	33	Z2-9a	S	Apatite	4962	11.01	0.026	7.57	2.23	16.43	0.79	3.94	0.18	6.09	Qiu et al. (2012)
	34	Z2-10a	S	Apatite	5138	4.01	0.01	1.02	12.77	12.67	0.73	1.76	0.2	15.75	Qiu et al. (2012)

Table 1 (continued)

Tectonic unit	No.	Samples	Strata	Mineral	Depth (m)	Mass (mg)	4He (nmol/g)	Th/U	U (ppm)	Th (ppm)	Ft	Corrected age (Ma)	Error (±1σ)	eU (ppm)	Data sources
	35	Z2-12a	O	Apatite	5462	3.67	0.005	20.45	9.03	180.09	0.71	0.33	0.07	51.36	Qiu et al. (2012)
	36	Z11-4a	C	Apatite	4181.56	1.75	0.007	4.26	14.21	59.06	0.65	1.8	0.13	28.09	Qiu et al. (2012)
	37	Z11-5a	D	Apatite	4351.5	6.8	0.0016	0.92	26.03	23.45	0.78	0.08	0.03	31.54	Qiu et al. (2012)
	38	Z11-7a	S	Apatite	4701.2	0.96	0.0043	1.24	62.47	75.36	0.59	0.77	0.11	80.18	Qiu et al. (2012)
	39	Z11-8a	S	Apatite	4922	1.3	0.0018	5.1	20.99	104.34	0.6	0.41	0.25	45.51	Qiu et al. (2012)
	40	Z11-10a	S	Apatite	5091	1.97	0.0026	18.35	14.08	251.84	0.63	0.23	0.1	73.26	Qiu et al. (2012)
Kongqiuhe slope	41	KQ1-1a	S	Apatite	2402.1	11.85	3.609	4.84	25.93	122.47	0.81	56.11	0.81	54.71	Qiu et al. (2012)
	42	KQ1-2a	S	Apatite	2593.8	3.4	0.0567	8.26	2.86	23.03	0.69	23.74	0.62	8.27	Qiu et al. (2012)
	43	KQ1-5a	S	Apatite	3201.5	5.29	0.432	3.91	9.96	37.96	0.75	46.57	0.73	18.88	Qiu et al. (2012)
	44	KQ1-7a	O	Apatite	4554.5	4.41	0.0232	1.3	3.22	4.06	0.74	13.84	0.54	4.17	Qiu et al. (2012)
	45	KQ1-1z1	S	Zircon	2402	1.91		0.73	281.19	200.51	0.68	398.05	11.58	328.31	Qiu et al. (2012)
	46	KQ1-2z1	S	Zircon	2593	7.93		2.95	34.12	98.01	0.783	408.93	7.25	57.16	Qiu et al. (2012)
	47	KQ1-3z1	S	Zircon	2799	4.59		0.68	74.32	49.42	0.765	547.48	12.18	85.94	Qiu et al. (2012)
	48	KQ1-4z2	S	Zircon	2956.5	2.17		0.69	189.44	127.59	0.706	529.94	12.89	219.42	Qiu et al. (2012)
	49	KQ1-5z2	S	Zircon	3201.5	7.46		0.77	139.87	104.38	0.791	438.38	10.28	164.4	Qiu et al. (2012)
	50	KQ1-6Z2	O	Zircon	4133.5	8.51		0.67	250.97	164.32	0.797	442.27	10.76	289.59	Qiu et al. (2012)
	51	KQ1-7z2	O	Zircon	4554.5	3.1		1.51	81.47	119.9	0.73	451.36	9.64	109.65	Qiu et al. (2012)
Bachu uplift	56	T1-1a	S	Apatite	1567.8	0.91	0.011	15.73	1.84	28.14	0.6	18.55	1.07	8.45	Qiu et al. (2011)
	57	T1-2a	S	Apatite	1694.3	0.9	0.1276	1.58	43.79	67.46	0.58	33.92	0.64	59.64	Qiu et al. (2011)
	58	T1-3a	S	Apatite	1791.5	3.24	0.03	0.67	16.01	10.49	0.72	5.68	0.17	18.47	Qiu et al. (2011)
	59	T1-4a	S	Apatite	1901.5	2.4	0.01	1.77	6.05	10.43	0.68	5.82	0.32	8.5	Qiu et al. (2011)
	60	T1-5a	S	Apatite	2095	2.46	0.335	17.67	18.84	324.57	0.67	17.5	0.28	95.12	Qiu et al. (2011)
	52	T1-5z2	S	Zircon	2095	1.83		0.43	138.41	58.34	0.714	368.95	11.35	152.12	Qiu et al. (2011)
	53	T1-7z2	∈	Zircon	4676	20.89		1.05	113.62	116.8	0.873	452.16	13.05	141.07	Qiu et al. (2011)
	54	T1-8z1	Z	Zircon	4707	5.65		0.97	94.39	89.32	0.794	333.95	9.54	115.38	Qiu et al. (2011)
	55	HT1-8z2	O	Zircon	4061.5	5.68		0.92	152.65	137.17	0.76	512.76	9.64	184.89	Qiu et al. (2011)
Tabei uplift	61	S14-7a	N	Apatite	2748	0.8	0.0346	2.43	2.54	6.02	0.601	147.21	8.76	3.96	Qiu et al. (2012)
	62	S14-10a	K	Apatite	3680	4.35	0.79	1.06	32.95	34.05	0.73	50	0.87	40.95	Qiu et al. (2012)
	63	S14-11a	K	Apatite	4015	2.94	0.064	0.65	18.91	11.99	0.708	11.67	0.31	21.73	Qiu et al. (2012)
	64	S14-12a	K	Apatite	4274	1.13	0.002	0.64	30.37	18.97	0.64	0.63	0.23	34.83	Qiu et al. (2012)
	65	S14-13a	J	Apatite	4550	2.04	0.05	0.28	12.16	3.34	0.683	22.22	0.61	12.94	Qiu et al. (2012)
	66	S14-14a	Tr	Apatite	4785	3.19	0.0014	3.03	3.66	10.82	0.698	0.85	0.28	6.2	Qiu et al. (2012)

Table 2 Geological information and results of apatite fission track from the Tarim Basin

Tectonic unit	No.	Well/Location	Stratum	Mineral	n	ρs (10⁵/cm²) (Ns)	ρi (10⁵/cm²) (Ni)	p(x²)	Mean age ±δ (Ma)	Central age ±δ (Ma)	Pool age ±δ (Ma)	L±1 σ/μm (N)	Data sources
Kongquehe slope	1	KQ1	S	Apatite	20	4.795 (486)	5.831 (591)	93.4		129±9		12.5±2 (102)	Qiu et al. (2012)
	2	KQ1	S	Apatite	21	6.26 (880)	10.763 (1513)	0		96±5		12.6±1.6 (105)	Qiu et al. (2012)
	3	KQ1	S	Apatite	20	7.745 (615)	11.911 (980)	21.7		103±6		10±2.9 (137)	Qiu et al. (2012)
	4	KQ1	S	Apatite	20	6.397 (593)	9.234 (856)	0		115±7		10±2.8 (116)	Qiu et al. (2012)
	5	KQ1	S	Apatite	21	4.65 (607)	8.25 (1077)	0		89±5		11.7±1.6 (104)	Qiu et al. (2012)
	6	KQ1	S	Apatite	21	5.586 (358)	9.627 (617)	97.1		92±7		12±1.7 (108)	Qiu et al. (2012)
	7	KQ1	O	Apatite	21	4.875 (311)	10.298 (657)	32.4		76±6		11.2±1.7 (104)	Qiu et al. (2012)
	8	KQ1	O	Apatite	20	3.122 (340)	9.209 (1003)	0		55±4		10.6±1.7 (106)	Qiu et al. (2012)
	9	KQ1	S	Apatite	28	5.724 (2026)	1.223 (433)	83.1	179±10	164±11	164±11	11.5±1.6 (100)	Xiao et al. (2011)
	10	KQ1	J	Apatite	28	6.899 (1960)	2.531 (719)	68.2	102±6	100±6	100±6	12.3±1.5 (99)	Xiao et al. (2011)
	11	YL1	J	Apatite	28	4.852 (985)	1.842 (374)	80.7	97±7	89±6	89±6	11.6±1.7 (101)	Xiao et al. (2011)
Tanggu depression	12	TC1	T	Apatite	54	13.06	10.5	0		238.6±15.4		11.2±1.4	Li et al. (2005)
	13	TC1	C	Apatite	27	2.39	4.83	0		96.5±8.9		9.8±1.4	Li et al. (2005)
	14	TC1	S	Apatite	55	2.99	6.49	0		104.5±12		9.6±1.4	Li et al. (2005)
Tazhong uplift	15	TZ12	P	Apatite	27	9.06	7.76	14		228.6±16		10.1±1.3	Li et al. (2005)
	16	TZ12	C	Apatite	27	2.72	4.75	0		113.8±13.4		9.8±1.4	Li et al. (2005)
	17	TZ12	S	Apatite	27	4.85	7.03	0		116.7±16.9		9.7±1.5	Li et al. (2005)
	18	TZ12	S	Apatite	26	4.02	9.02	0		88.9±13.3		9.4±1.5	Li et al. (2005)
	19	TZ12	S	Apatite	27	2.02	6.06	0		66±11.3		9.9±1.6	Li et al. (2005)
	20	TZ45	T	Apatite	23	10.34	8.61	0.6		232.7±16		12±1.3	Li et al. (2005)
	21	TZ45	P	Apatite	16	5.35	16.36	0		157.7±32.4		11.5±1.5	Li et al. (2005)
	22	TZ45	C	Apatite	20	2.8	5.59	5.3		99±9.8		9.0±1.5	Li et al. (2005)
	23	TZ45	D	Apatite	28	4.21	9.16	0		92.8±12.8		8.8±1.3	Li et al. (2005)
	24	TZ45	S	Apatite	29	2.61	7.92	0		73.3±14		10.6±1.4	Li et al. (2005)
	25	TZ8	C	Apatite	28	3.237 (966)	1.28 (382)	47.5		86±7	87±6	9.9±1.8 (98)	Xiang et al. (2013)
	26	TZ6	C	Apatite	28	5.72 (1878)	3.73 (1225)	0		51±5	50±3	10.3±2.0 (105)	Xiang et al. (2013)
	27	TZ8	C	Apatite	28	1.02 (442)	1.389 (602)	52.9		28±2	28±2	9.8±1.7 (75)	Xiang et al. (2013)
	28	TZ6	C	Apatite	28	1.052 (528)	1.735 (871)	83.1		25±2	25±2	9.7±1.7 (80)	Xiang et al. (2013)
	29	TZ6	S	Apatite	25	1.819 (573)	2.923 (921)	0		28±2	25±2	10.1±1.7 (38)	Xiang et al. (2013)
	30	TZ18	T	Apatite	20	5.673 (1916)	1.655 (559)	72.2		108±7	108±7	12.2±2.0 (105)	Xiang et al. (2013)
	31	TZ401	C	Apatite	22	5.79 (802)	2.83 (392)	88.3		80±6	80±6	10.7±1.6 (49)	Xiang et al. (2013)
	32	TZ401	C	Apatite	27	1.2 (400)	1.22 (406)	82.8		36±3	37±3	9.6±2.0 (63)	Xiang et al. (2013)

Table 2 (continued)

Tectonic unit	No.	Well/Location	Stratum	Mineral	n	ρs (10⁵/cm²) (Ns)	ρi (10⁵/cm²) (Ni)	p(x²)	Mean age ±δ (Ma)	Central age ±δ (Ma)	Pool age ±δ (Ma)	L±1 σ/μm (N)	Data sources
	33	TZ401	C	Apatite	28	1.89(594)	1.29(406)	0.3		57±6	53±4	9.4±2.0(104)	Xiang et al. (2013)
	34	TZ401	C	Apatite	28	3.49(952)	1.972(538)	7.4		67±6	64±4	9.3±1.7(81)	Xiang et al. (2013)
	35	TZ10	T	Apatite	27	5.854(3047)	2.106(1096)	3.4		105±6	104±5	12±1.6(96)	Xiang et al. (2013)
	36	TZ10	T	Apatite	28	7.859(3087)	2.2(864)	33.7		133±7	132±7	11.5±1.5(98)	Xiang et al. (2013)
Bachu uplift	37	F1	D	Apatite		1.89(68)	19.76(899)	>30		24.8±2.0		N.D.	Qiu et al. (2010)
	38	F1	D	Apatite		2.46(200)	11.65(946)	<0.1		66.6±7.5		10.2±2.1(62)	Qiu et al. (2010)
	39	H3	S	Apatite		8.84(821)	27.44(2549)	<0.1		75.1±10.6		10.0±1.9(116)	Qiu et al. (2010)
	40	H3	S	Apatite		15.1(435)	39.41(1135)	<0.1		143.7±22.1		10.0±1.7(76)	Qiu et al. (2010)
	41	H3	S	Apatite		1.34(27)	2.43(49)	>80		141.5±33.6		10.9±1.8(56)	Qiu et al. (2010)
	42	H4	D	Apatite	12	6.29(39)	30.65(190)	>50		53.1±9.3		N.D.	Qiu et al. (2012)
	43	H4	S	Apatite	10	4.44(326)	17.81(1309)	<0.1		75.7±14.2		10.4±2.3(50)	Qiu et al. (2012)
	44	H4	S	Apatite	5	4.24(228)	19.89(1070)	<0.1		63.1±9.2		11.6±2.2(6)	Qiu et al. (2012)
	45	T1	E	Apatite	28	5.919(647)	12.46(1362)	69.6		94±7		11.8±1.8(87)	Qiu et al. (2012)
	46	T1	S	Apatite	24	4.294(225)	11.471(601)	99.89		74±7		13.9±0.9(4)	Qiu et al. (2012)
	47	T1	S	Apatite	28	3.597(609)	7.781(1285)	67.5		90±6		12.1±1.9(99)	Qiu et al. (2012)
	48	T1	S	Apatite	29	3.09(609)	7.047(1389)	98.3		85±6		11.7±2.2(105)	Qiu et al. (2012)
	49	T1	Z	Apatite	30	0.633(131)	1.933(400)	98.03		62±7		N.D.	Qiu et al. (2012)
	50	HT1	D	Apatite	28	0.984(234)	9.013(2144)	7.82		19±2		N.D.	Qiu et al. (2012)
	51	HT1	S	Apatite	29	1.773(326)	7.899(1452)	0		41±6		10.9±1.8(45)	Qiu et al. (2012)
	52	HT1	O	Apatite	31	1.537(324)	12.287(2675)	0		24±3		10.7±1.6(29)	Qiu et al. (2012)

ρs=spontaneous track density; ρi=induced track density in the external detector (muscovite), all track densities are $10^5/cm^2$. Ns=the numbers of spontaneous track; Ni=the numbers of induced track. n=the number of tracks measured. $P(x^2)$=chi-square probability, which is a measure of probability that individual grains counted in a sample are from a single population. Ages were determined using average age when $P(x^2) < 5\%$, which are generally taken to indicate that multiple age population is present. However, ages were determined using assembled age with the $P(x^2) > 5\%$. Mean track lengths are corrected for length bias (Laslett et al. 1982)
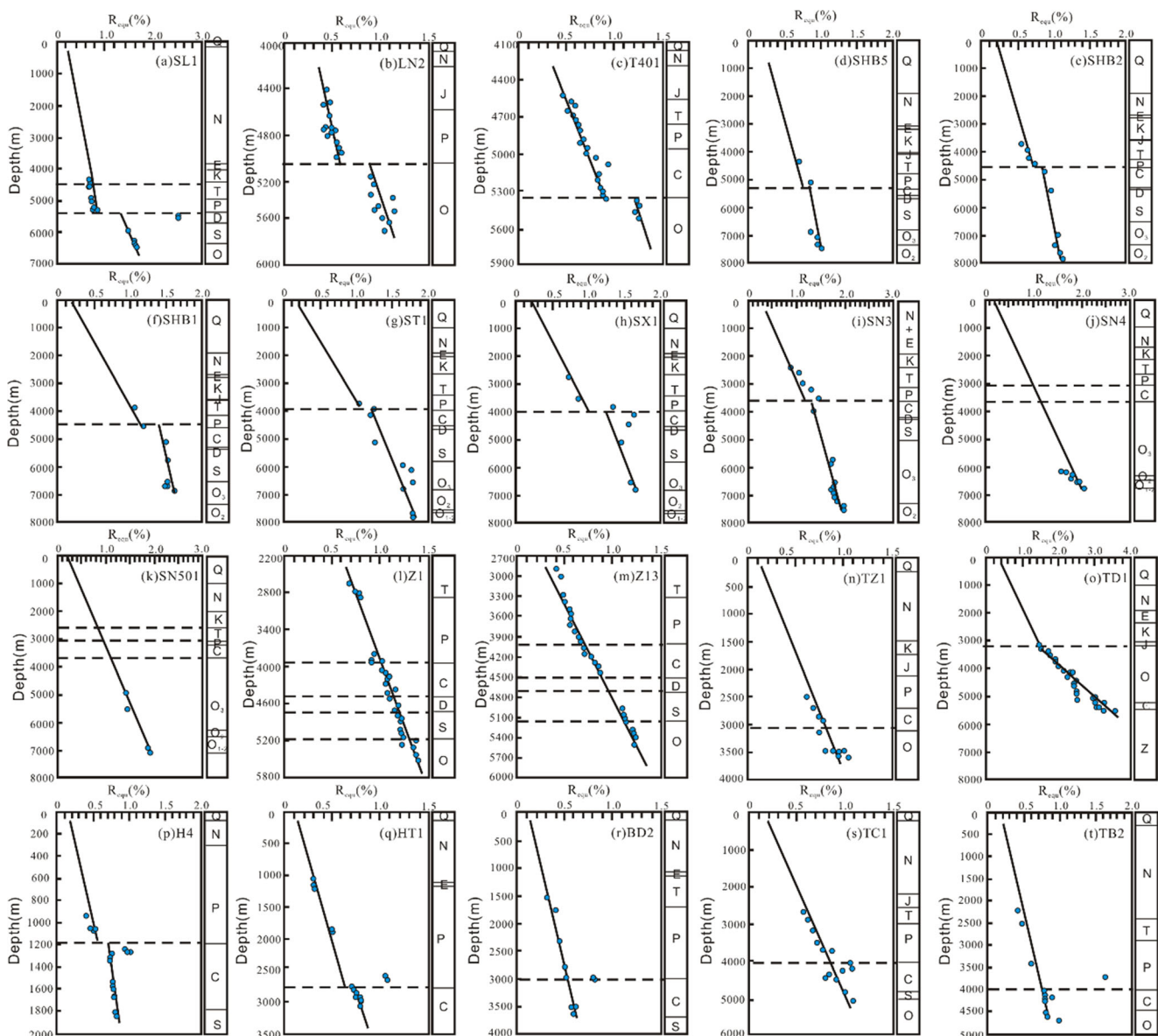
Fig. 2 Requ versus depth of typical wells in Tarim Basin. (**a**)–(**c**): The wells of SL1, LN2, and T401 represent the Tabei uplift, and these data are from Liu et al. (2016); (**d**)–(**k**): The wells of SHB5, SHB2, SHB1, ST1, SX1, SN3, SN4, and SN501 represent the Shuntuoguole low uplift, and these data are from this study; (**l**)–(**n**): The wells of Z1, Z13, and TZ1 represent the Tazhong uplift, and these data are from this study and Wang et al. (2010); (**o**): The well of TD1 represent the Tadong uplift, and these data are from Qiu et al. (2012); (**p**)–(**q**): The wells of H4 and HT1 represent the Bachu uplift, and these data are from Li et al. (2016); (**s**)–(**t**): The wells of TC1 and TB2 represent the Tanggu depression, and these data are from Li et al. (2016)

Results

Analytical results of paleo-thermal indicators

Equivalent vitrinite reflectance (Requ)

The Requ value is controlled by the heating temperature and heating time of the organic matter, and is mainly affected by temperature (Buchardt and Lewan 1990; Burnham and Sweeney 1989). In the tectonically stable state, Ro and depth show a linear relationship (Barker et al. 1986; Barker and Goldstein 1990; Sweeney and Burnham 1990), whereas in the case of strata erosion and unsteady high heat source intrusion, it will lead to the offset of the Requ-depth profile. In the Tarim Basin, the equivalent vitrinite reflectance profiles (%Requ) from 20 wells all show increasing trends with depth (Fig. 2). The Requ values of Tabei uplift (Fig. 2a–c), Shuntuoguole low uplift (Fig. 2d–i), Bachu uplift (Fig. 2p–q), and Tanggu depression (Fig. 2s–t) are discontinuous in the Permian and Pre-Permian, and there are many sporadic extremely high Ro anomalies near the unconformity surface, recording obvious tectonic heat. The event revealed that the

Fig. 3 (**a**) Relationship between zircon He age and the grain radius; (**b**) Relationship between zircon He age and eU concentration; (**c**) Relationship between zircon He age and the ^{4}He concentration
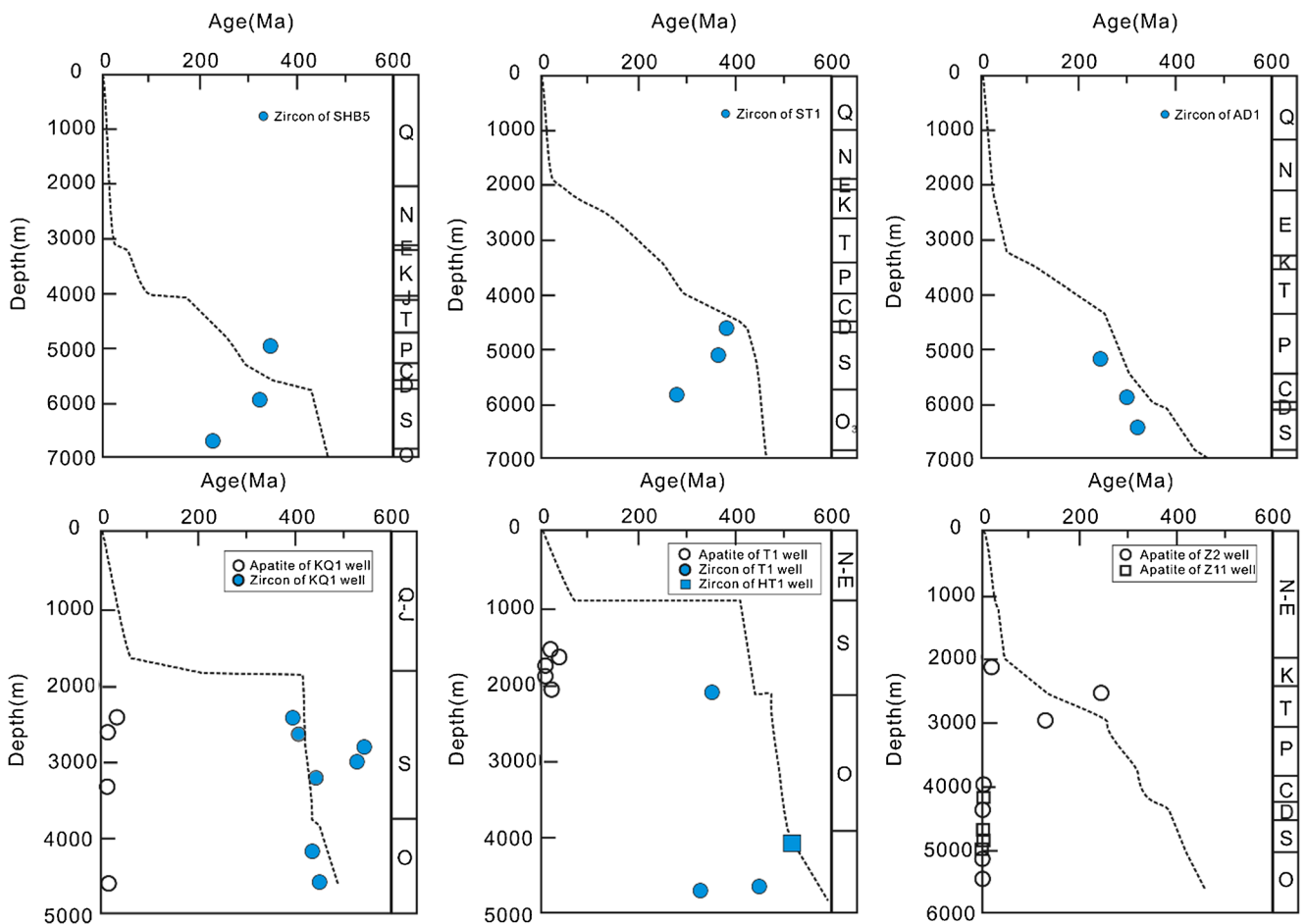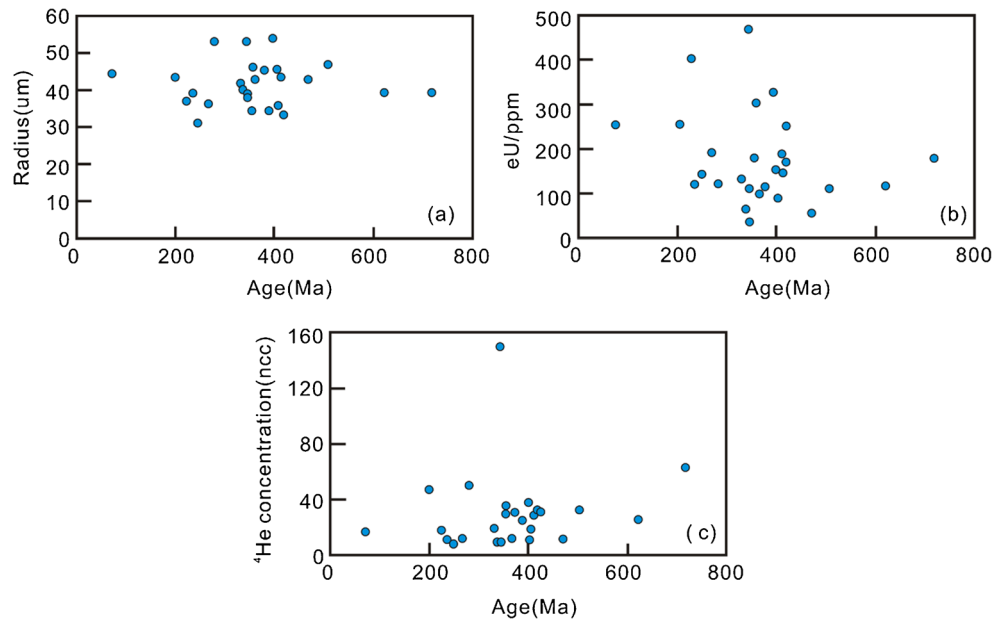
Fig. 4 Relationship between (U–Th)/He ages of apatite and zircon and burial depth for typical wells in the Tarim Basin (dashed line indicates the stratigraphic age, the data of SHB5, ST1, and AD1 wells are from this study, and the data of KQ1, T1, HT1, Z2, and Z11 wells are from Qiu et al. (2012))

end of the Carboniferous strata experienced a higher paleotemperature (Li et al. 2010; Zhu et al. 2016a; Zhu et al. 2016b).

(U–Th)/He ages for apatite and zircon

Zircon and apatite (U–Th)/He results are shown in Table 1. The ZHe ages of nine zircon grains of well SHB5, ST1, and AD1 are from this study, and ZHe ages range from 71.1±4.4 to 717.4±44.5 Ma, but some samples had a large variation among the single-grain ZHe ages. Previous studies believed that the main factors affecting the variation of He ages in the intra-sample included the crystal size (Reiners and Farley 2001), effective Uranium (Farley et al. 1996), and radiation damage (Shuster et al. 2006; Flowers et al. 2007) (Fig. 3). The grain size directly affects the diffusion loss of ^{4}He. The larger the zircon grain size, the more ^{4}He concentration will be preserved. However, some grains with higher He ages have smaller grain radius (such as AD1-4c and SHB5-4c), and these abnormal particles should be excluded for thermal history recovery. In addition, excess He is another key factor in the variation of He ages, in grains ST1-6a and SHB5-4c, and the ^{4}He value is extremely high whereas the eU is relatively

low, suggesting there was significant "parentless" ^{4}He in these grains, and thus they also should be excluded. After removing the outliers, suitable samples were selected for analysis. The age of zircon He gradually decreases with the increase of stratum age except for SHB5-2a, and the zircon He ages are slightly smaller than the age of stratum (Fig. 4a–c). These findings suggest that these zircon samples are partially reset, and the highest temperature experienced entering a partial retention zone of zircon He age. In the well of KQ1, the apatite He ages are between 13.84 and 56.11 Ma, and these He ages are much younger than their stratigraphic ages, which implies that these apatite samples of Silurian and Ordovician strata are almost entirely reset. The zircon (U–Th)/He ages decrease with the depth of samples, and the Zhe ages of the Ordovician samples are slightly younger than their depositional ages, which implies that the highest temperature experienced by the Ordovician strata enters a partial retention zone of zircon He age (Fig. 4d). In the wells of T1, HT1, Z2, and Z11, the apatite and zircon He ages are also younger than the stratigraphic ages, indicating heating to high temperatures (Fig. 4e–f). Therefore, the maximum temperature experienced by the sample can be effectively constrained in the thermal history simulation.

Fig. 5 Relationships between AFT ages, lengths, and strata of different tectonic units in the Tarim Basin. (These data are from Qiu et al. (2010); Xiang et al. (2013); Chang et al. (2014a, b); Qiu et al. (2012) and Xiao et al. (2011))
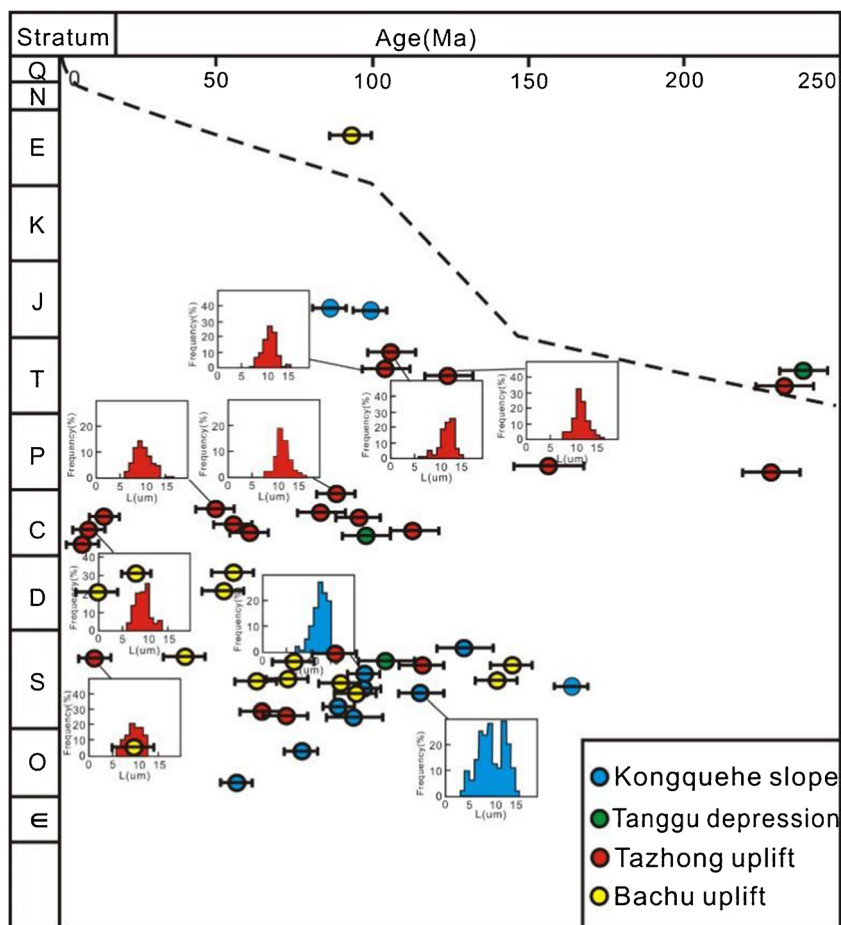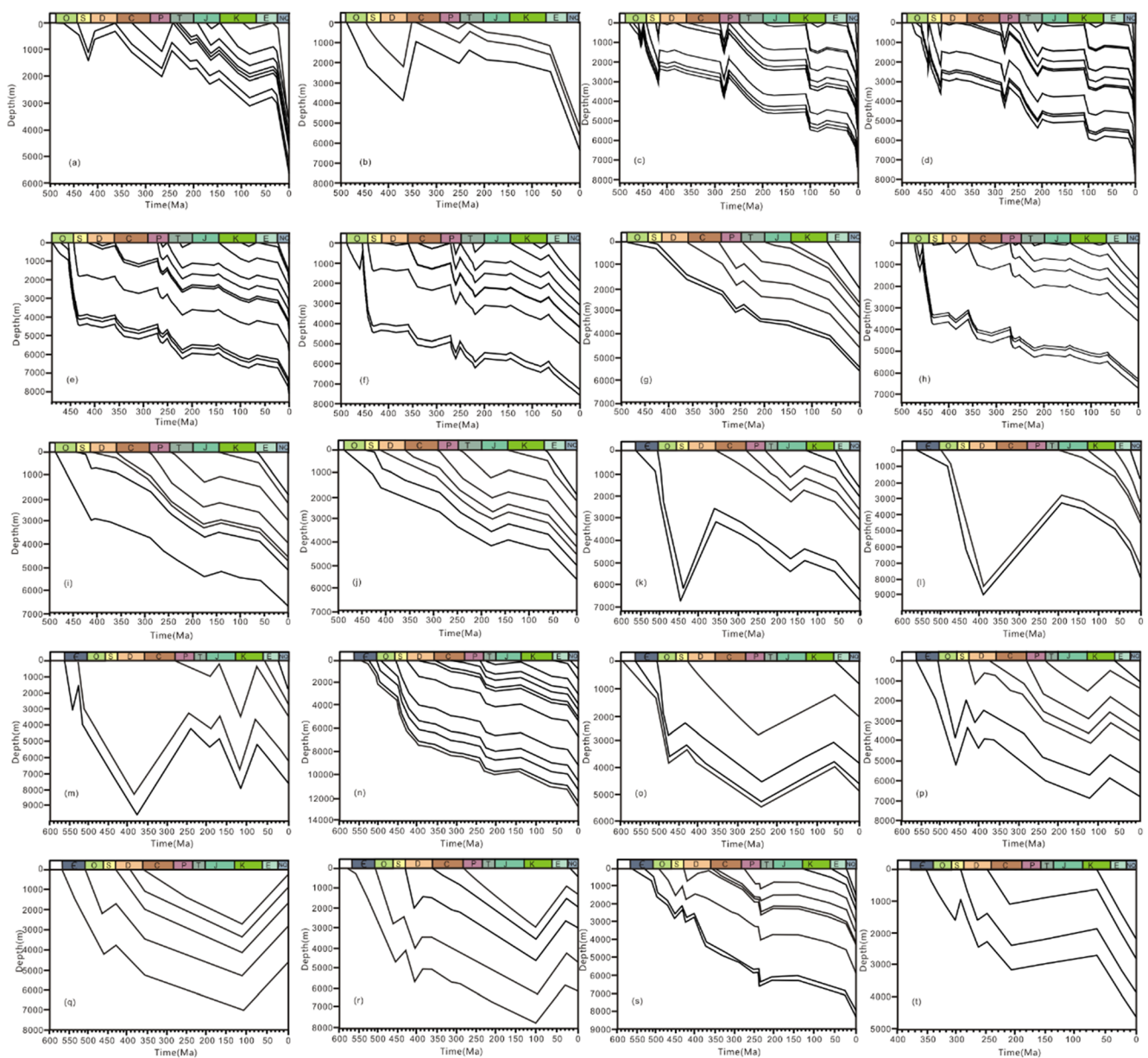
Fig. 6 Burial history of different tectonic units in the Tarim Basin. (**a**)–(**b**): The wells of LN2 and T401 are modified after Chen et al. (2014) and Sun (2017); (**c**)–(**h**): The wells of SHB5, SHB2, ST1, SN3, and SN4 are from this study; (**i**)–(**k**): The wells of Z2, Z11, and TZ1 are modified after Wang et al. (2010); (**l**): The well of TD1 is modified after Wang et al. (2003); (**m**): The well of KQ1 is modified after Qiu et al. (2012); (**n**)–(**r**): The wells of MC1, F1, T1, HT1, and H4 are modified after Qiu et al. (2011) and Qiu et al. (2010); (**s**)–(**t**): The wells of TC1 and TB2 are modified after Li et al. (2016)

Fission tracks for apatite and zircon

Fifty-two fission-track (FT) ages have been previously determined from the Kongquehe slope, Bachu Uplift, Tanggu depression, and Tazhong uplift (Table 2; Fig. 5). In general, the AFT central ages in the Tarim Basin are variable, ranging from 19.0 ± 2.0 Ma (HT1) and 25.0 ± 2.0 Ma (TZ6) to 232.7 ± 16.0 Ma (TZ45). Except for these three samples (T1, TZ45, TC1), the other AFT ages or age pattern are considerably younger than depositional or stratigraphic ages, indicating that the apatites in the detrital samples have

undergone significant post depositional annealing and resetting. In Kongquehe slope, the AFT data sets all show that the AFTs have partially annealed. The AFT ages decrease from 164 Ma for the Upper Silurian sample to 55 Ma for the Ordovician sample. In the Bachu uplift, Tanggu depression, and Tazhong uplift, the AFT ages also decrease with increasing depth, and their AFT ages are younger than the corresponding stratigraphic ages of Paleozoic–Mesozoic strata, which suggest that these samples had partially annealed.

The mean track lengths of these samples vary from 8.8 μm (TZ45) to 12.6μm (KQ1) with corresponding standard

deviation of 0.9 to 2.9 μm. Specifically, the values of mean track lengths in the Tazhong uplift (from 9.4 μm to 12.0 μm) are all less than 12.0 μm, shorter than those of the Kongquehe slope (from 10.0 μm to 12.6 μm) and Bachu uplift (from 10.0 μm to 12.1 μm). These track lengths are evidently

smaller than the standard of unannealed mean track lengths of 16.3 ± 0.9 μm (Gleadow et al. 1986). The track length distribution (Fig. 5) of most samples exhibit the signature of a typical "mixed" distribution pattern (Gleadow et al. 1986). From the "mixed" type of length distribution illustrated above,
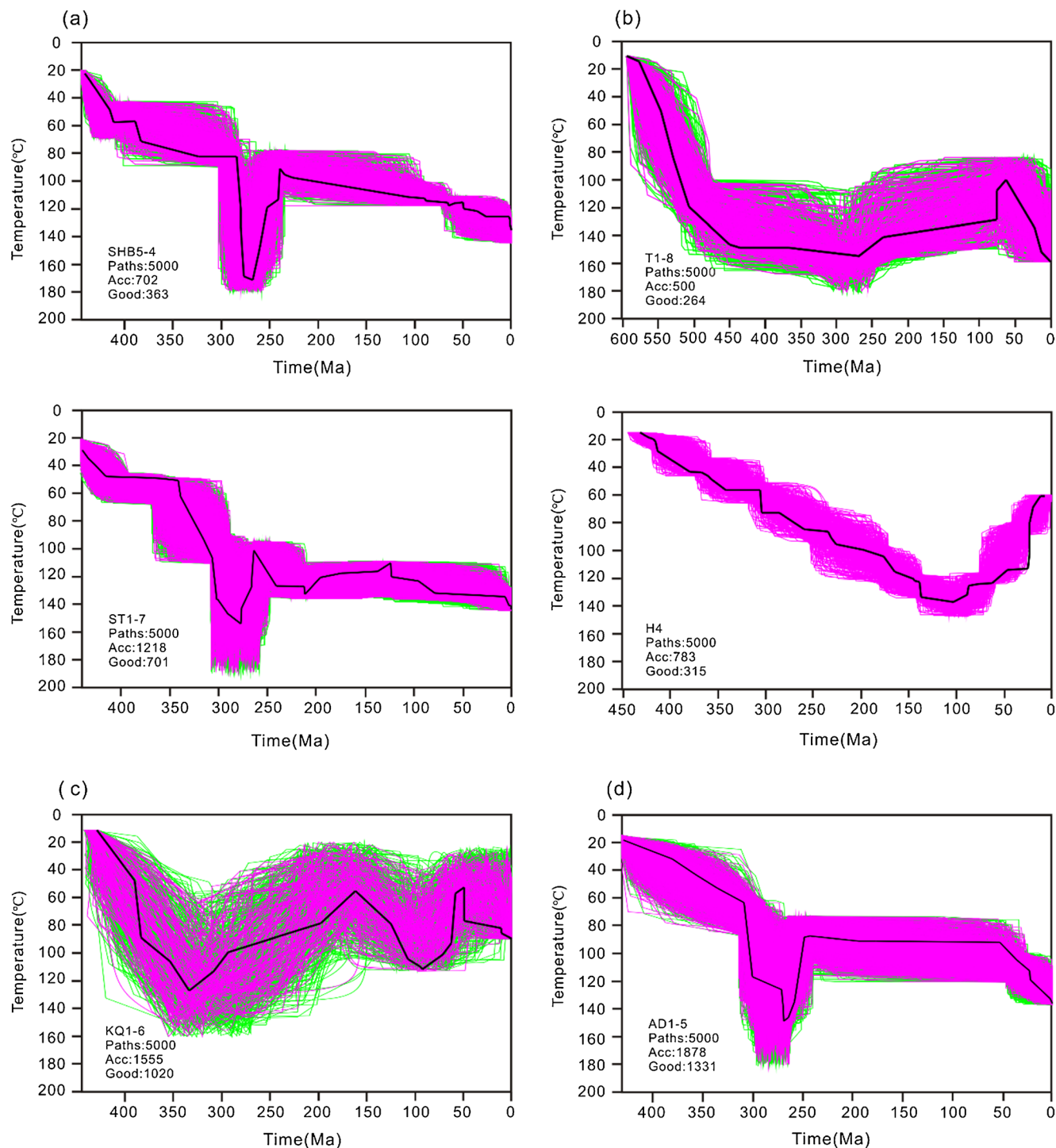
Fig. 7 Thermal history (t-T) histories of the Tarim Basin samples based on AFT ages and length data, Requ data, and (U–Th)/He ages using HeFty program. (**a**) Shuntuoguole low uplift, including SHB5, and ST1. (**b**) Bachu uplift, including T1 and H4. (**c**) Kongquehe slope, including KQ1 well. (**d**) Awati sag, including AD1 well. The results in the t-T curves show three reliability paths, that is, green = acceptable fit, magenta=good fit, and black = best fit

we can conclude that samples were probably affected by a multistage thermal history, in which some tracks have been thermally shortened while others have been generated by subsequent cooling (Gleadow et al. 1986).

Model results

Burial history reconstruction

Burial-history reconstruction is the basis for the reconstruction of thermal history. To construct burial histories, thickness, depths, and average lithology data in the wells referred to the well completion reports provided by previous studies. Erosion events and the according eroded thickness are site-specific, and were thus considered separately (Chen et al. 2014; Sun 2017; Wang et al. 2003, 2010; Qiu et al. 2010, 2011, 2012; Li et al. 2016). The burial histories show that in the Tabei and Tazhong uplift, these areas are almost continuously subsiding since the Cambrian period, and the current stratum depth is the largest depth. However, the Tadong uplift and Bachu uplift underwent a large scale of uplift. The Hercynian and Indosinian orogenies were dominant factors in the tectonic transformation of the eastern Tarim Basin. The Yanshanian and Himalayan orogenies resulted in rapid uplift and sedimentation in the Tarim Basin during the Mesozoic–Cenozoic (Fig. 6).

Thermal history modeling

In order to better restore the thermal history of the Tarim Basin, based on the analysis of the characteristics of the paleo-thermal indicators, (U–Th)/He ages, FT ages, and equivalent vitrinite reflectance (Requ) were combined and used to reconstruct the thermal history for Tarim Basin. The software HeFTy (version 1.9.1) was applied to model the thermal histories. In our modeling, 5000–10,000 thermal paths were developed using the Monte Carlo inverse-

modeling method, and the best-fit time-Temperature (t-T) path model indicated the thermal history of the sample. The thermal history of six typical drilling samples was modeled from different tectonic units (Fig. 7). In Shuntuoguole low uplift, the modeling results of the samples SHB5-4 and ST1-7 show that this area gradually warmed up during the Late Sinian to Devonian phase reaching approximately 80–90 °C, then the temperature began to rise rapidly and the peak paleo-temperature appeared in the Early Permian, reaching 160–170°C. The formation temperature then rapidly cooled and returned to normal thermal conditions during the Middle Permian. After the Early Permian, the formation temperature slowly increased and the current temperature has reached 120–140 °C (Fig. 7a). In Bachu uplift and Kongquehe slope, the thermal models show that these samples underwent first an overall heating stage after their deposition until the Devonian period, then followed by two major cooling episodes which could be recognized from the t-T paths. These two cooling events are closely related to the tectonic activities of Hercynian and Yanshanian in the Tarim Basin (Fig. 7b and Fig. 7c). In Awati sag, the thermal models showed a very similar thermal history with Shuntuoguole area. During the Late Permian, the samples reached a maximum paleotemperature of approximately 140–160 °C. Then it began to cool down rapidly and returned to normal thermal state during the middle-late Permian (Fig. 7d).

Using the thermal conductivity (K) (Liu et al. 2020a), the general paleo heat flow (q) history of the deep boreholes in the Tarim Basin is shown (q=−K• Gt) in Fig. 8. The value of heat flow in the Tarim Basin has almost continuously decreased during the entire geologic history. While the heat flow evolved differently in the different structural zones. Higher heat flow exists in the Tadong and Tazhong uplift than in the Bachu uplift, Tabei uplift, and Shuntuoguole low uplift (Fig. 8). In general, there are three phases of heat flow evolution in the Tarim Basin: (1) The gradual cooling stage during Ordovician-Carboniferous, the heat flow is gradually

Fig. 8 Heat flow histories of different structural zones in the Tarim Basin
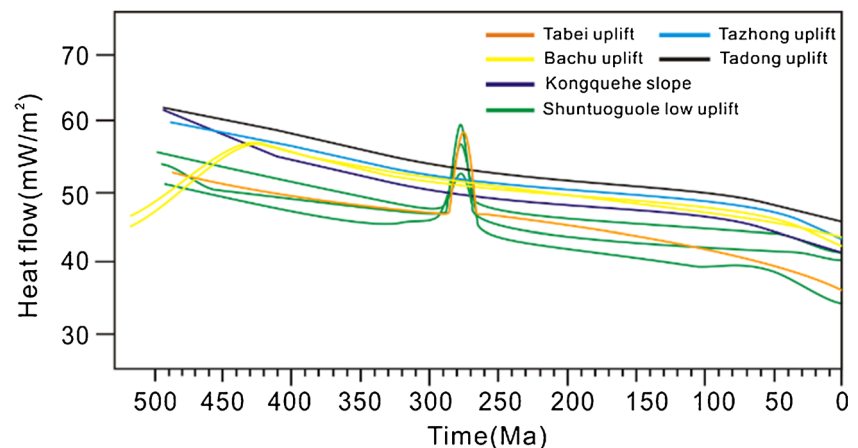
decreasing during this period; (2) Rapidly raised stage in the early Permian period, the heat flow in Tabei and Tazhong uplift are raised rapidly during this period and the maximum is 51~62mW/m^2; (3) The decline stage since Middle Permian. The tectonic activity is relatively stable and the geothermal heat flow is gradually reduced during this period.

The maturity of the source rocks

The maturation histories of the source rocks control the timing of hydrocarbon generation and expulsion (Pang et al. 2012; Carminati et al. 2010; Kosakowski and Krzywiec 2013; Hudson and Hanson 2010). The maturity histories of the Cambrian–Ordovician source rocks were calculated based on the newly obtained Requ data and ZHe data of Shuntuoguole low uplift, and the maturities of the source rock for the other wells were taken from Qiu et al. (2012). The division of mature evolution stages of source rocks is an indispensable reference premise for the research of maturity history, and the value of Requ was used to indicate the stage of the maturity history classified as follows: Immaturity stage (Requ < 0.5%); Early maturation stage, (0.5% < Requ < 0.7%); Middle maturation stage, (0.7% < Requ < 1%); Late maturation stage, (1% < Requ < 1.3%); Main-gas stage, (1.3% < Requ < 2%).

The modeling results show (Fig. 9) that the maturation of the source rocks in different areas underwent different maturation evolutions. In the well of SHB2, SHB5, and ST1, the Lower Cambrian and Lower Ordovician source rocks entered the Early maturation stage (0.5%<Ro<0.7%) and began to form hydrocarbons since the Caledonian period. At the end of the Early Permian, under the abnormal heat flow of magmatic activity, the maturity of the source rock was rapidly

entered the main-gas stage (1.3% <Ro < 1.5%) (Fig.9a–b). In the well of SN3, SN501, and SN2, the maturity of the Lower Cambrian and Lower Ordovician source rocks reached the hydrocarbon generation threshold in the middle Caledonian period. During the Hercynian–Yanshan–Hishan period, the maturity of the Lower Cambrian and Lower Ordovician source rocks gradually increased. The Lower Cambrian source rocks reached the stage of dry gas generation (>2%), and the Lower Ordovician source rocks reached the high maturity stage (1.3% < Requ < 2%) (Fig. 9c–e). According to the occurrence state of hydrocarbons and the maturity evolution of Lower Ordovician and Lower Cambrian source rocks, it can be seen that the degree of the lower Cambrian source rocks is well matched with the distribution of oil and gas reservoir types in Shuntuogule low uplift. Therefore, only from the perspective of source rock evolution, the main source rock in the Shuntoguole area of Tarim Basin may be the Lower Cambrian source rock.

According to the thermal evolution results of the source rocks recovered by single wells, the Kriging interpolation method was used to simulate the maturity evolution plane distribution of the bottom interface of the Lower Cambrian source rock. The maturation modeling results indicated that by the end of the Ordovician, the bottom of Cambrian entered the generation threshold (0.5% Ro). Mainly, early mature source rock existed in the Bachu uplift and Tabei uplift, and the middle and late mature source rocks were distributed in the Northern uplift, the Tanggu depression, Tazhong uplift, and the Kongquehe slope. The source rock reached the main gas stage in the eastern region of the basin, and it was at the dry gas stage in the Manjiaer depression (Fig. 10a). By the end of the Permian, the source rock intervals which had reached the main gas stages covered most of the basin, except the Tabei
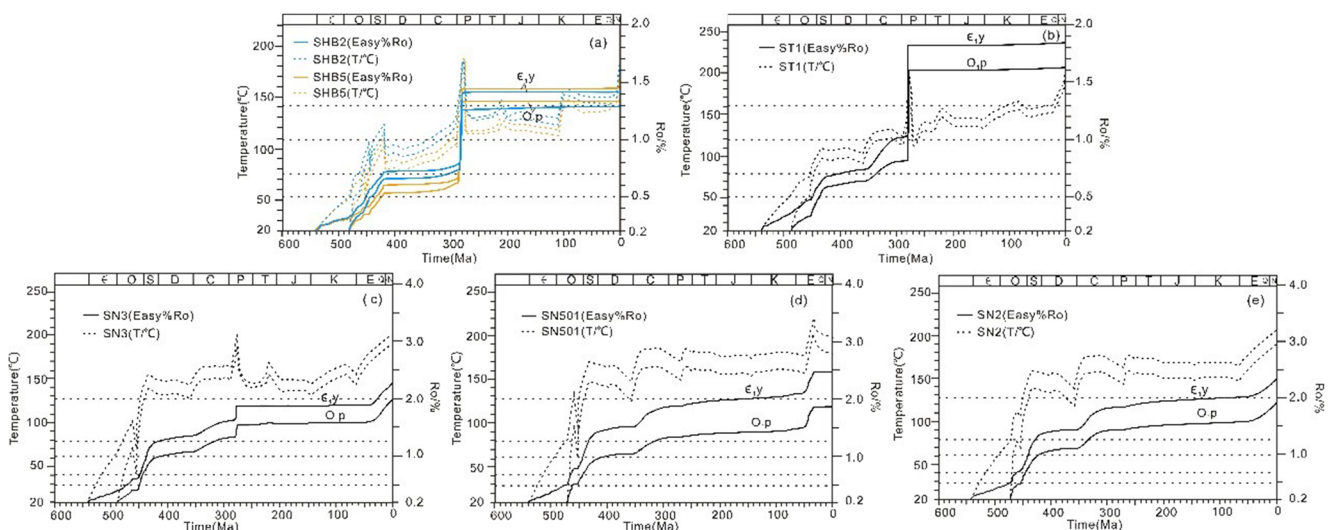

Fig. 9 Thermal evolution of source rocks for the typical drilling source rocks in the Tarim Basin
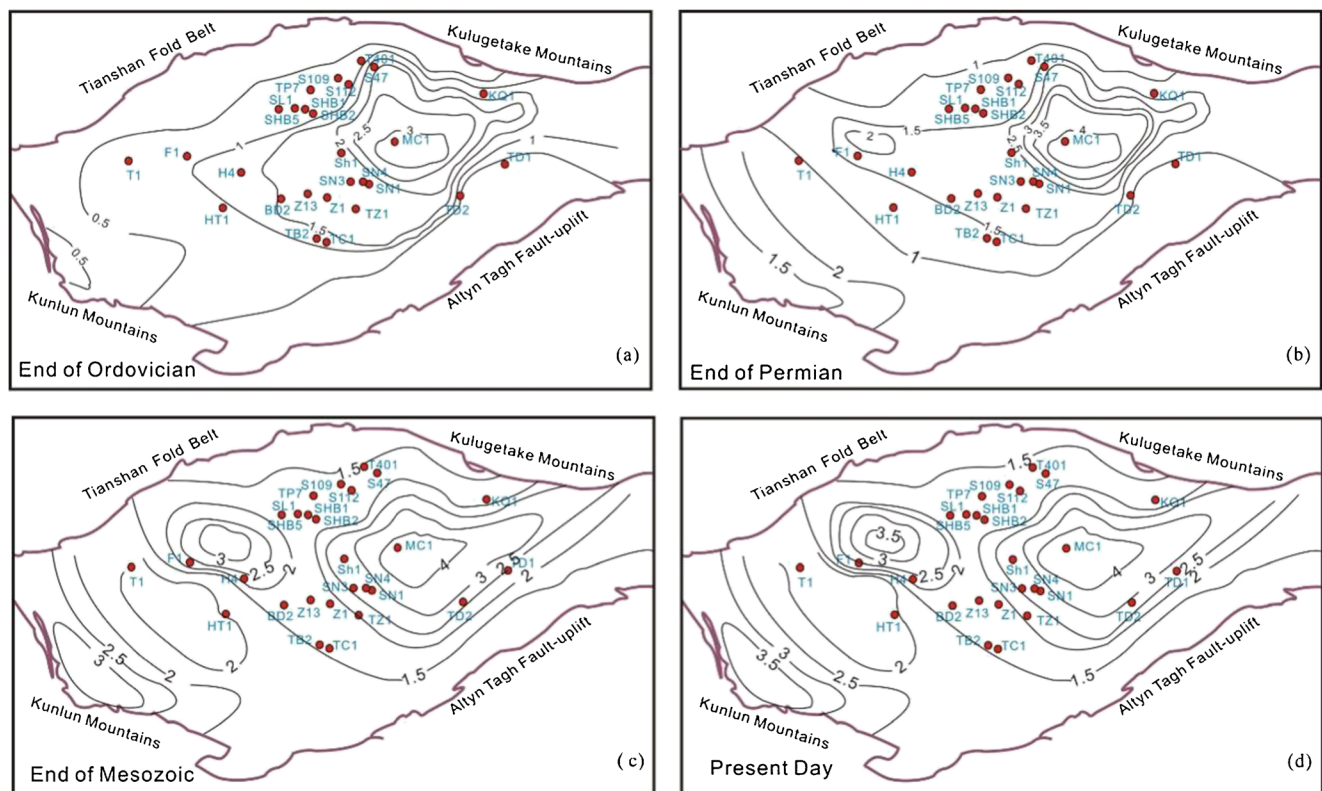
Fig. 10 Maturation level of the bottom interface of the Lower Cambrian source rock. The contour interval is 0.5%. Requ = equivalent vitrinite reflectance (modified after Qiu et al. 2012; Yang et al. 2020)

uplift, Bachu uplift, and the southern part of the Southwest depression, where the source rocks were still within the oil window (Requ < 1.3%) (Fig. 10b). By the end of the Mesozoic, the dry gas stage was mainly distributed in the south of Shuntuoguole low uplift, Manjiaer depression, Tadong uplift, and Kongquehe slope (Fig. 10c). Currently, the maturity mostly maintained the characteristics of the end of the Mesozoic (Fig. 10d).

Discussion

The limitations of the paleo-temperature indicators

Although the various paleo-temperature indicators have their own advantages, they also have some limitations in the restoration of thermal history. Vitrinite reflectance is the most commonly used paleo-temperature method for thermal history research, and it can be used to objectively characterize the organic matter maturity of source rocks since the Late Paleozoic. However, for the early Paleozoic marine strata, due to the lack of vitrinites from higher plants, some other organic matter maturity indicators (asphalt reflectance and vitrinite-like reflectance) are usually converted into equivalent vitrinite

reflectance in order to recover the thermal history. However, the organic matter paleo-temperature indicators as the highest paleo-thermometer, which can only record the highest paleo-temperature experienced in the geological history period, the paleo-temperature information recorded before this period will be erased, and the subsequent lower temperature information cannot be recorded.

The apparent age of low-temperature thermochronology has no direct geological significance in many cases. Only when the sample is continuously cooled in a linear manner can its apparent age be interpreted as the time when the sample passes its sealing temperature. Therefore, when analyzing the low-temperature thermochronological samples, it is necessary to combine other information to constrain their ages. In addition, the pre-processing of low-temperature thermochronology samples is more complicated and cumbersome. Laser etching-ICPMS will become a mainstream method of apparent age testing and analysis. The development of other paleo-temperature scales, such as the concentration of organic matter free radicals and rock thermoacoustic emission lacks effective quantitative models to model the thermal histories of the sedimentary basins. Therefore, a single paleo-temperature scale method may lead to uncertainty and diversification of the thermal history recovery results. Multiple

Fig. 11 The evolution of mantle plume in the Tarim Basin from 310 to 290Ma and the geothermal gradient distribution during the Permian period
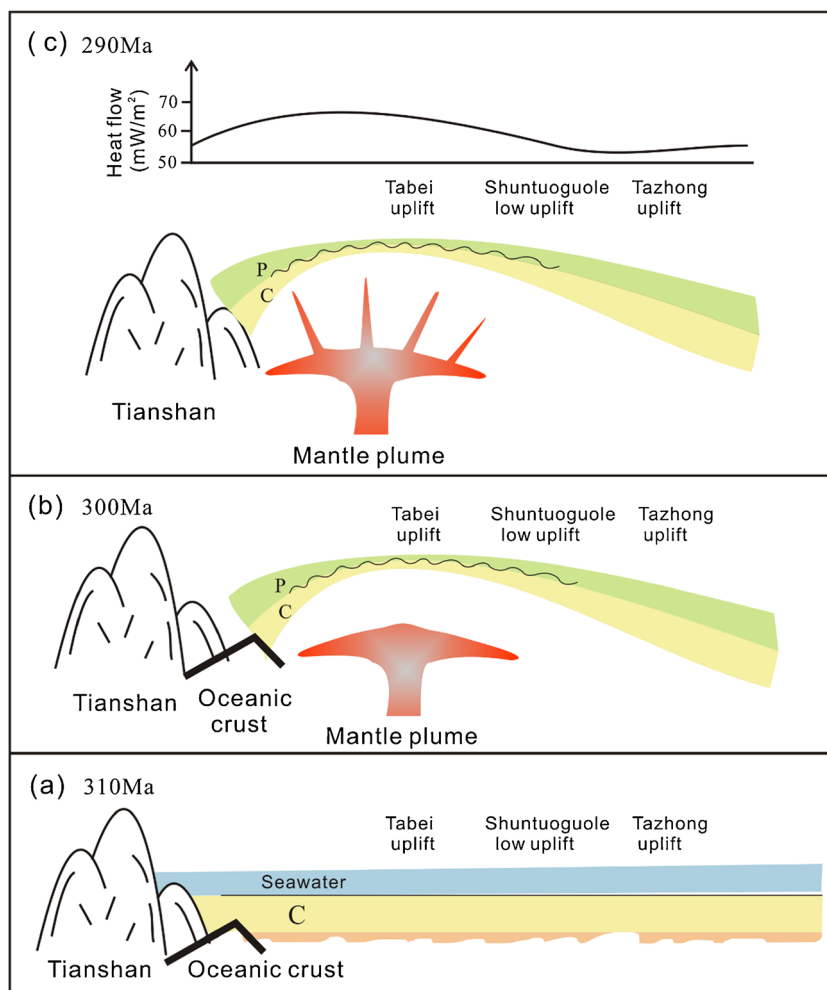
ancient temperature scale methods (organic matter paleo-- temperature, low-temperature thermochronological ancient temperature, etc.) should be combined with each other to take advantage of each other's advantages.

Relationship between the thermal history and tectonic evolution

Generally, thermal evolution is controlled by the tectonic setting. The Tarim Basin was a stable craton basin during the Paleozoic (Jia and Wei 2002), and the stretching and thinning of the crust resulted in a higher geothermal gradient at that time. During the Permian, the heat flow began to increase and during the Middle-Late Permian, reached a peak value in Tabei and Tazhong uplift. Li et al. (2016) indicated that the heat flow peak in the Tarim Basin was mainly controlled by the magmatic activity which created a thermal pulse. We calculated the maximum geothermal gradients for each well at the time of peak burial temperature. The results show that the maximum geothermal gradients

have a range of 26.75°C/km to 46.28°C/km and exhibit a southward decreasing trend. Such high calculated geothermal gradients clearly indicating a thermal pulse which probably was related to the magmatic activity as suggested by some researchers (Li et al. 2010; Li et al. 2016). The well log section of the Tabei and Tazhong area also shows that magmatic rocks are generally developed in the Permian, and the thickness of the magmatic rocks in the northern area is thicker than that in the southern area (Liu et al. 2020b). A mantle plume was assigned to be origin of Large Igneous Province in Tarim basin (Yang et al. 2013; Li et al. 2014; Xu et al. 2014), is generally characterized by a wide lateral expanse, can vertically affect the geothermal regime over a large area (Gouveia et al. 2018), and thus could be regarded as a plausible heating source. The nearby Sichuan basin, which has similar tectonic history with Tarim basin, is well-recognized for Permian mantle plume activity and is a good example for comparison. Geothermal studies in Sichuan basin have revealed a high thermal anomaly induced by mantle plume and generate geothermal gradients

up to > 40°C/km, with gradients the highest in the center of mantle plume and decrease away from the center (Zhu et al. 2016a, b; Jiang et al. 2018). For the Tarim basin, the calculated geothermal gradients closely resemble those in Sichuan basin influenced by mantle plume. And the spatial pattern of peak burial temperature and geothermal gradients in this study corresponds to the distribution of Large Igneous Province (LIP). These pieces of evidence all support the hypothesis of a thermal pulse resulting from mantle plume activity in the Tarim basin. The spatial variation of calculated geothermal gradients would also illustrate that the center of the mantle plume to be near the Tabei area, consistent with previous research (Li et al. 2014), and the lateral extent of thermal influence exerted by mantle plume could be in the Tazhong uplift.

Through sedimentary stratigraphic studies, it is determined that the crust uplifted rapidly before the magmatic activity. The strong uplift occurred at ~300Ma, which caused the unconformity between the Carboniferous and Permian. Large-scale magmatic activity is between 300 and 288 Ma (Xu et al. 2014; Li et al. 2014). The heat flow began to rise rapidly, and the degree of thermal exhibits a southward decreasing trend. The degree of stratum denudation during this period also tended to gradually decrease from north to south. Therefore, the abnormally high paleo-temperature in the Permian period may be caused by magmatic activity and structural uplift. After 290 Ma, most of the heat generated by the mantle plume disappeared, and the geothermal gradient began to rapidly decrease and returned to a normal thermal state. The subsequent geothermal gradient was mainly controlled by the depth of the stratum (Fig. 11).

Conclusions

(1) The thermal history of the Tarim Basin was reconstructed integrating multiple thermal indicators as follows: He ages, Fission tracks, and Requ data. The modeled results showed that the Tarim Basin underwent a gradual cooling stage during Ordovician-Carboniferous. During the early Permian period, the heat flow rapidly increased and reached a peak value (51–62 mW/m²) in Tabei and Tazhong uplift, and then decreased since Middle Permian. After the Middle Permian, the tectonic activity was relatively stable and the geothermal heat flow was gradually reduced during this period.

(2) The maturity histories of the source rocks, modeled based on the new thermal histories, indicate that the maturation of the source rocks in different areas underwent different maturation evolutions. The Cambrian source rocks experienced rapid burial and heating during the Caledonian period, entered the hydrocarbon generation stage during the end of Ordovician, and at the end of

Mesozoic, the Cambrian source rocks reached the dry gas stage in the south of Shuntuoguole low uplift, Manjiaer depression, Tadong uplift, and Kongquehe slope. Currently, the maturity mostly maintained the characteristics of the end of the Mesozoic.

Declarations

Conflict of interest The authors declare that they have no known competing financial interests or personal relationships that could have appeared to influence the work reported in this paper.

References

Bai GP, Cao BF (2014) Characteristics and distribution patterns of deep petroleum accumulations in the world. Oil Gas Geol 35(1):19–25 (in Chinese with English Abstract)

Bao J, Zhu C, Wang Z (2018) Typical end-member oil derived from Cambrian-Lower Ordovician source rocks in the Tarim Basin, NW China. Pet Explor Dev 45(6):1177–1188

Barker CE, Goldstein RH (1990) Fluid-inclusion technique for determining maximum temperature in calcite and its comparison to the vitrinite reflectance geothermometer. Geology 18(10):1003–1006

Barker C, Pawlewicz M, Buntebarth G et al (1986) The correlation of vitrinite reflectance with maximum temperature in humic organic matter. In: Paleogeothermics. Springer, Berlin Heidelberg, pp 79–93

Buchardt B, Lewan M (1990) Reflectance of vitrinite-like macerals as a thermal maturity index for Cambrian-Ordovician Alum Shale, Southern Scandinavia. AAPG Bull 74(4):394–406

Burnham AK, Sweeney JJ (1989) A chemical kinetic model of vitrinite maturation and reflectance. Geochim Cosmochim Acta 53(10): 2649–2657

Cai C, Zhang C, Worden RH et al (2015) Application of sulfur and carbon isotopes to oil–source rock correlation: a case study from the Tazhong Area, Tarim Basin, China. Org Geochem 83:140–152

Carminati E, Cavazza D, Scrocca D et al (2010) Thermal and tectonic evolution of the southern Alps (northern Italy) rifting: coupled organic matter maturity analysis and thermokinematic modeling. AAPG Bull 94:369–397

Chang J, Brown RW, Yuan WM et al (2014a) Mesozoic cooling history of the "Bachu Uplift" in the Tarim Basin, China: constraints from zircon fission-track thermochronology. Radiat Meas 2014(67):5–14

Chang X, Wang TG, Li Q et al (2014b) Charging of Ordovician reservoirs in the Halahatang Depression (Tarim Basin, NW China) determined by oil geochemistry. J Pet Geol 36(4):383–398

Chen H, Wu Y, Feng Y et al (2014) Timing and chronology of hydrocarbon charging in the Ordovician of Tahe oilfield, Tarim Basin, NW China. Oil Gas Geol 35(6):806–819

Chen Z, Wang TG, Li M, Yang F, Cheng B (2018) Biomarker geochemistry of crude oils and Lower Paleozoic source rocks in the Tarim Basin, western China: an oil-source rock correlation study. Mar Pet Geol 96:94–112

Ding CH, Zhou HB, Lu P et al (2009) The Paleozoic structural features and its evolution in the Tazhong low uplift, Xinjiang. Geotecton Metallog 33(1):148–153 (In Chinese)

Dyman TS, Crovelli RA, Bartberger CE et al (2002) Worldwide estimates of deep natural gas resources based on the U.S. Geological Survey World Petroleum Assessment. Nat Resour Res 11(3):207–218

Farley K (2000) Helium diffusion from apatite: general behavior as illustrated by Durango fluorapatite. J Geophys Res 105:2909–2914

Farley KA, Wolf RA, Silver LT (1996) The effects of long alpha-stopping distances on (U-Th)/He ages. Geochim Cosmochim Acta 60:4223–4229

Flowers RM, Shuster DL, Wernicke BP et al (2007) Radiation damage control on apatite (U-Th)/He dates from the Grand Canyon region, Colorado Plateau. Geology 53:447–450

Gleadow A, Harrison M, Kohn B, Lugo-Zazueta R, Phillips D (2015) The fish canyon tuff: a new look at an old low-temperature thermochronology standard. Earth Planet Sci Lett 424:95–108

Gleadow AJW, Duddy IR, Green PF, Lovering JF (1986) Confined fission track lengths in apatite: a diagnostic tool for thermal history analysis. Contrib Mineral Petrol 94(4):405–415

Gouveia DSV, Besse J, deLamotte DF et al (2018) Evidence of hotspot paths below Arabia and the Horn of Africa and consequences on the Red Sea opening. Earth Planet Sci Lett 487:210–220

Hudson SM, Hanson AD (2010) Thermal maturation and hydrocarbon migration within La Popa Basin, northeastern Mexico, with implications for other salt structures. AAPG Bull 94:273–291

Jacbo H (1989) Classification, structure, genesis and practical importance of natural solid oil bitumen ("migrabitumen"). Int J Coal Geol 11:65–79

Jia CZ (1997) Tectonic characteristics and petroleum Tarim basin China. Petroleum industry press, Beijing, pp 1–274 (in Chinese)

Jia C, Wei G (2002) Structural characteristics and petroliferous features of Tarim Basin. Chin Sci Bull 47(1):1–11

Jiang Q, Qiu N, Zhu C (2018) Heat flow study of the Emeishan large igneous province region: implications for the geodynamics of the Emeishan mantle plume. Tectonophysics 724:11–27

Ketcham RA, Carter A, Donelick RA, Barbarand J, Hurford AJ (2007) Improved modeling of fission-track annealing in apatite. Am Mineral 92(5-6):799–810

Kosakowski P, Krzywiec PM (2013) Modelling hydrocarbon generation in the Palaeozoic and Mesozoic successions in SE Poland and West Ukraine. J Pet Geol 36:139–161

Laslett GM, Kendall WS, Gleadow AJW, Duddy IR (1982) (1982) Bias in measurement of fission-track length distributions. Nucl Tracks Radiat Meas 6(2–3):79–85

Li HL, Qiu NS, Jin ZJ et al (2005) Thermal history of Tarim Basin. Oil Gas Geol 26:613–617 (in Chinese with English abstract)

Li M, Wang TG, Chen JF, He F, Yun L, Akbar S, Zhang W (2010) Paleo-heat flow evolution of the Tabei Uplift in Tarim Basin, northwest China. J Asian Earth Sci 37(1):52–66

Li CX, Wang XF, Li BL, He D (2013) Paleozoic fault systems of the Tazhong uplift, Tarim Basin. China. Mar Pet Geol 39(1):48–58

Li D, Yang S, Chen H, Cheng X, Li K, Jin X, Li Z, Li Y, Zou S (2014) Late Carboniferous crustal uplift of the Tarim plate and its constraints on the evolution of the Early Permian Tarim Large Igneous Province. Lithos 204:36–46

Li S, Amrani A, Pang X, Yang H, Said-Ahmad W, Zhang B, Pang Q (2015) Origin and quantitative source assessment of deep oils in the Tazhong uplift, Tarim Basin. Org Geochem 78:1–22

Li JW, Li Z, Qiu NS et al (2016) Carboniferous-Permian abnormal thermal evolution of the Tarim basin and its implication for deep structure and magmatic activity. Chin J Geophys 59(9):3318–3329

Liu DH, Shi JY (1994) Study on the evaluation methods on high matured carbonate source rocks. Pet Explor Dev 21:113–115 (in Chinese with English abstract)

Liu YJ, Neubauer F, Genser J, Ge XH, Takasu A, Yuan SH, Chang LH, Li WM (2007) Geochronology of the initiation and displacement of the Altyn Strike-Slip Fault, western China. J Asian Earth Sci 29(2-3):243–252

Liu SW, Lei X, Feng CG, Hao C (2016) Estimation of subsurface formation temperature in the Tarim Basin, northwest China: implications for hydrocarbon generation and preservation. Int J Earth Sci 105:1329–1351

Liu W, Qiu N, Xu Q et al (2018) Precambrian temperature and pressure system of Gaoshiti-Moxi block in the central paleo-uplift of Sichuan basin, southwest China. Precambrian Res 33:91–108

Liu Y, Qiu N, Hu W, Li H, Shen F, Yao Q (2019) Temperature and pressure characteristics of Ordovician gas condensate reservoirs in the Tazhong area, Tarim Basin, northwestern China. AAPG Bull 103(6):1351–1381

Liu Y, Qiu N, Li H et al (2020a) Terrestrial heat flow and crustal thermal structure in the northern slope of Tazhong uplift in Tarim Basin. Geothermics 83:1–14

Liu YC, Qiu NS, Chang J et al (2020b) Application of clamped isotope thermometry to thermal evolution of sedimentary basins: a case study of Shuntuoguole in Tarim Basin. Chin J Geophys 63(2):597–611

Ma Q, Lü H, Jiang H et al (2015) Division program of structural units in the Paleozoic platform-basin region, Tarim Basin. Marine Orig Petrol Geol 20(1):1–9

Mu SL (2009) Exploration theory, technology and practice for oil and gas in China's marine strata: Beijing, China, vol 752. Geological Publishing House

Pang XQ, Liu KY, Ma ZZ et al (2012) Dynamic field division of hydrocarbon migration, accumulation and hydrocarbon enrichment rules in sedimentary basins. Acta Geol Sin 86:1559–1592

Petersen HI, Sherwood N, Mathiesen A, Fyhn MBW, Dau NT, Russell N, Bojesen-Koefoed JA, Nielsen LH (2009) Application of integrated vitrinite reflectance and FAMM analyses for thermal maturity assessment of the northeastern Malay Basin, offshore Vietnam: implications for petroleum prospectivity evaluation. Mar Pet Geol 26:319–332

Qi LX (2016) Oil and gas breakthrough in ultra-deep Ordovician carbonate formations in Shuntuoguole uplift, Tarim Basin. China. Petrol Explor 21(3):38–51 (Chinese)

Qiu NS, Jiang G, Mei QH et al (2010) Tectono-thermal evolution in the Bachu Uplift, Tarim Basin, China. Acta Geol Sin-Engl Ed 84:1286–1293

Qiu NS, Jiang G, Mei QH, Chang J, Wang S, Wang J (2011) The Paleozoic tectonothermal evolution of the Bachu Uplift of the Tarim Basin, NW China: constraints from (U–Th)/He ages, apatite fission track and vitrinite reflectance data. J Asian Earth Sci 41(6):551–563

Qiu NS, Chang J, Zuo YH et al (2012) Thermal evolution and maturation of lower Paleozoic source rocks in the Tarim Basin, northwest China. AAPG Bull 96(5):789–821

Reiners PW, Farley KA (2001) Influence of crystal size on apatite (U-Th)/He thermochronology: an example from the Bighorn Mountains: Wyoming. Earth Planet Sci Lett 188:413–420

Reiners PW, Spell TL, Nicolescu S, Zanetti KA (2004) Zircon (U-Th)/He thermochronometry: He diffusion and comparisons with ^{40}Ar/^{39}Ar dating. Geochim Cosmochim Acta 68:1857–1887

Ren JY, Zhang JX, Yang HZ et al (2011) Analysis of fault systems in the Central uplift, Tarim Basin. Acta Petrol Sin 27(1):219–230

Ren JY, Yang HZ, Hu DS et al (2012) Fault activity and its controlling to marine cratonic breakup in Tarim Basin. Earth Sci 37(4):645–653

Shuster DL, Flowers RM, Farley KA (2006) The influence of natural radiation damage on helium diffusion kinetics in apatite. Earth Planet Sci Lett 249:148–161

Sun Y (2017) Hydrocarbon accumulation period of Triassic reservoirs in Lunnan and surrounding area of Tarim Basin.

Sun YS, Jin YA, Gu QY et al (2003) Timing of paleo-oil accumulation in Tadong No. 2 Well, Tarim Basin. Pet Explor Dev 30(5):31–33 (in Chinese with English abstract)

Sweeney JJ, Burnham AK (1990) Evaluation of a simple model of vitrinite reflectance based on chemical kinetics. AAPG Bull 10(10):1559–1570

Tang LJ, Jia CZ, Jin ZJ, Chen SP, Pi XJ, Xie HW (2004) Salt tectonic evolution and hydrocarbon accumulation of Kuqa foreland fold belt, Tarim Basin, NW China. J Pet Sci Eng 41:97–108

Wang F, Zhang S, Zhang B et al (2003) Maturity and its history of Cambrian marine source rocks in the Tarim Basin. Geochimica 32(5):461–468

Wang YP, Zhang SC, Wang FY, Wang Z, Zhao C, Wang H, Liu J, Lu J, Geng A, Liu D (2006) Thermal cracking history by laboratory kinetic simulation of Paleozoic oil in eastern Tarim Basin, NW China, implications for the occurrence of residual oil reservoirs. Org Geochem 37:1803–1815

Wang TG, Dai SF, Li MJ, Zhang WB, Qiu NS, Wang GL (2010) Stratigraphic thermohistory and its implications for regional geoevolution in the Tarim Basin, NW China. Sci China Earth Sci 53:1495–1505

Wang TG, Song DF, Li MJ et al (2014) Natural gas source and deep gas exploration potential of the ordovician yingshan formation in the shunnan-gucheng region, Tarim basin. Oil & Gas Geology 035(006):753–762

Wu L, Guan SW, Ren R et al (2016) The characteristics of Precambrian sedimentary basin and the distribution of deep source rock: a case study of Tarim Basin in Neoproterozoic and source rocks in Early Cambrian, Western China. Pet Explor Dev 43(6):905–915

Xiang C, Pang X, Danisík M (2013) Post-triassic thermal history of the Tazhong uplift zone in the Tarim Basin, northwest China: evidence from apatite fission-track thermochronology. Geosci Front 6:743–754

Xiao XM, Wilkins RWT, Liu DH et al (2000) Investigation of thermal maturity of lower Paleozoic hydrocarbon source rocks by means of vitrinite like maceral reflectance: a Tarim Basin case study. Org Geochem 31:1041–1052

Xiao H, Ren ZL, Wang QC et al (2011) Detrital zircon and apatite fission track study of key tectonic events of Kongquehe slope and Kuruketage uplift, north–eastern Tarim Basin, China. Chin J Geophys 54:817–827 (in Chinese with English abstract)

Xiong R, Zhou J, Ni X et al (2015) Distribution prediction of Lower Cambrian Yuertusi Formation source rocks and its significance to oil and gas exploration in the Tarim Basin. Nat Gas Ind 35(10):49–56

Xu YG, Wei X, Luo ZY, Liu HQ, Cao J (2014) The Early Permian Tarim Large Igneous Province: main characteristics and a plume incubation model. Lithos 204:20–35

Yamada R, Murakami M, Tagami T (2007) Statistical modeling of annealing kinetics of fission tracks in zircon: Reassessment of laboratory experiment. Chem Geol 236:95–122

Yan L, Yang M, Zhang J et al (2020) Distribution of Cambrian source rocks and evaluation and optimization of favorable zones in East Tarim Basin. Nat Gas Geosci 31(5):667–674

Yang SF, Chen HL, Ji DW et al (2005) Geological process of early to middle Permian magmatism in Tarim Basin and its geodynamic significance. Geol J China Univ 11(4):504–511 (In Chinese)

Yang S, Chen H, Li Z, Li YQ, Yu X, Li DX, Meng LF (2013) Early Permian Tarim large igneous province in northwest China. Sci China Earth Sci 56(12):2015–2026

Yang P, Wu G, Ren Z et al (2020) Tectono-thermal evolution of Cambrian–Ordovician source rocks and implications for hydrocarbon generation in the eastern Tarim Basin, NW China. J Asian Earth Sci 194:1–15

Yao G, Wu X, Sun Z et al (2018) Status and prospects of exploration and exploitation key technologies of the deep petroleum resources in onshore China. J Nat Gas Geosci 3(1):25–35 (Chinese)

Yu BS, Zhou LF (2005) Distribution of hydrocarbon source rocks of Cambrian-Ordovician in sequence stratigraphic framework in Tarim Basin. Chin J Geophys 1(1):59–61

Yu J, Zhang J, Shi B (2010) A study on tectono-thermal evolution history of Bachu uplift in the Tarim Basin. Chin J Geophys 53(5):805–814

Zhang BM, Zhang SC, Yin LM et al (2005) Bioprecursors of the Lianglitake-type source rocks from the Late Ordovician of Tarim Basin (in Chinese). Acta Micropaleontol Sin 22:243–250

Zhang S, Huang H, Su J, Zhu G, Wang X, Larter S (2014) Geochemistry of paleozoic marine oils from the Tarim Basin, NW China. Part 4: paleo-biodegradation and oil charge mixing. Org Geochem 67:41–57

Zheng J, Li B, Liu Y et al (2018) Study on thermal evolution modeling of lower Cambrian Yuertusi source rock, Tarim Basin. Reserv Rval Develop 8(6):7–12 (In Chinese)

Zhou X, Lü X, Quan H, Qian W, Mu X, Chen K, Wang Z, Bai Z (2019) Influence factors and an evaluation method about breakthrough pressure of carbonate rocks: an experimental study on the Ordovician of carbonate rock from the Kalpin area, Tarim Basin, China. Mar Pet Geol 104:313–330

Zhu G, Chen F, Chen Z, Zhang Y, Xing X, Tao X, Ma D (2016) Discovery and basic characteristics of high-quality source rocks found in the Yuertusi formation of the Cambrian in Tarim Basin, China. J Nat Gas Geosci 1:21–33

Zhu C, Hu S, Qiu N et al (2016a) Thermal history of the Sichuan basin, SW China: evidence from deep boreholes. Sci China Earth Sci 59(1):70–82 (in Chinese with English abstract)

Zhu C, Hu S, Qiu N et al (2016b) Geothermal constraints on Emeishan mantle plume magmatism: paleotemperature reconstruction of the Sichuan basin, SW China. Int J Earth Sci 107:71–88

Zhu G, Cao Y, Yan L (2018) Potential and favorable areas of petroleum exploration of ultra-deep marine strata more than 8000 m deep in the Tarim Basin, Northwest China. J Nat Gas Geosci 3(6):321–337